Electronic Supplementary Information

A Self-Assembled Metallo-Macrocycle Two-Qubit Spin System

Gordon J. Douglas,[a] *Emma Richards*[b] *and Stephen Sproules**[a]

[a] School of Chemistry, University of Glasgow, Glasgow G12 8QQ (UK)

[b] School of Chemistry, Cardiff University, Main Building, Park Place, Cardiff CF10 3AT (UK)

Experimental Section

Synthesis. All air-sensitive materials were manipulated using standard Schlenk techniques or a glovebox. The complex [Cu(dbdtc)$_2$] (dbdtc = dibenzyl dithiocarbamato) was prepared following the procedure of Ajibade et al.[1] All reagents were commercially obtained and used as received.

Synthesis of [Cu$_2$(L)$_2$], [1]. To isopropylamine (5.00 mL; 58.2 mmol) in 20 mL THF was added portionwise α,α′-dibromo-*m*-xylene (1.00 g; 3.79 mmol), and stirred at ambient temperature for 2 h. The precipitate that evolved was removed by filtration, and the filtrate was reduced to a colourless oil under vacuum. The oil was reconstituted in 2:1 THF/water (60 mL), treated with triethylamine (950 mg; 9.39 mmol) and stirred for 10 min. This was followed by addition of carbon disulfide (712 mg; 9.39 mmol) which produced a clear yellow solution after 10 min. Copper acetate (950 mg; 4.75 mmol) was added and the reaction mixture left the stir for 18 h. A black precipitate was collected by filtration and washed with MeOH (10 mL), then Et$_2$O (10 mL). Recrystallisation was achieved by dissolving in CH_2Cl_2 (200 mL) and layered with EtOH (300 mL). The dark brown microcrystalline solid was isolated by filtration, washed with MeOH and dried under vacuum. Yield: 367 mg (22%). Anal. Calcd for $C_{32}H_{44}N_4S_4Cu_2$: C, 44.29; H, 5.07; N, 6.46. Found: C, 44.12; H, 5.09; N, 6.44. IR (KBr / cm^{-1}): 2972 m, 2934 w, 1506 m, ν(C–N) 1466 s, 1445 s, 1420 s, 1381 w, 1364 w, 1352 m, 1329 m, 1261 m, 1227 m, 1159 s, 1128 m, 1113 w, 1088 w, 1063 s, ν(C–S) 964 s, 910 w, 880 w, 777 m, 735 m, 694 m, 656 m. Absorption spectrum (CH_2Cl_2; λ_{max} / nm (ε / 10^{-4} M^{-1} cm^{-1})): 432 (1.90), 510 (sh, 0.23), 606 (0.19). ESI mass spectrum (pos. ion): *m*/*z* 890 [M+Na]$^+$.

EPR Spectroscopy. Continuous wave X-band EPR spectra was recorded on a Bruker ELEXSYS E500 spectrometer. Spectra were simulated using the simulation package XSOPHE.[2] Fluid solution spectra were simulated using a spin Hamiltonian of the form $\hat{H} = g\cdot\mu_B\cdot B\cdot S + \Sigma a\cdot S\cdot I$, where the weighted summation is over all naturally occurring Cu isotopes. Satisfactory fits were achieved using a Lorentzian lineshape with molecular tumbling accommodated by the isotropic liquids model given by $\sigma_v = a + bM_I + cM_I^2 + dM_I^3$. The simulation of the frozen solution spectrum for [Cu(dbdtc)$_2$] was achieved using the spin-Hamiltonian $\hat{H} = \mu_B\mathbf{B}\cdot\mathbf{g}\cdot\mathbf{S} + \mathbf{S}\cdot\mathbf{A}\cdot\mathbf{I} - \mu_n g_n\mathbf{B}\cdot\mathbf{I}$, where **g** and **A** are the 3×3 electron Zeeman and magnetic hyperfine interaction matrices,

respectively, and the last term is the nuclear Zeeman interaction. A Gaussian lineshape and distribution of *g*- and *A*-values (strain) were employed to account for the linewidth variation.

Pulsed X-band EPR data were measured using a Bruker ELEXSYS E580 spectrometer equipped with an Oxford Instruments CF935 continuous Helium flow cryostat. The sample was prepared by dissolving [**1**] in 4:1 $CDCl_3/Cl_3CCN$ to a concentration of 0.5 mM and loading into a 3.8 mm o.d. quartz EPR tube. The solution sample was degassed via three freeze-pump-thaw cycles, followed by flame sealing. ESE-detected EPR spectra were collected at 10 K using a Hahn echo pulse sequence ($\pi/2 - \tau - \pi - \tau -$ echo) with a 4-step phase cycle, where $\pi/2$ = 16 ns, π = 32 ns and τ = 400 ns. Simulations were performed as using XSOPHE[2] using the aforementioned spin-Hamiltonian. Phase memory times (T_M) were also measured with a Hahn echo pulse sequence. Decay curves were collected at field positions indicated on ESE spectra. Acquisition times were set to capture the top half of the spin echo and the acquired echo was integrated to obtain the spectrum. The data were phased by maximizing the sum of the data points in the real components of the spectrum and fit to the biexponential function $I(\tau) = y_0 + A_f \exp(-\tau/T_{M,f}) + A_s \exp(-\tau/T_{M,s})$, where f and s indicate fast and slow processes, respectively. Spin-lattice relaxation times (T_1) were collected at 10 K following the inversion recovery sequence ($\pi - T - \pi/2 - \tau - \pi - \tau -$ echo) with 4-step phase cycling in which $\pi/2$ = 16 ns, π = 32 ns, and T incremented from a starting value of 100 ns. The value of τ was selected to correspond to the maximum in the ESEEM at 400 ns. Acquisition times were set to capture the top half of the spin echo and the acquired echo was integrated to obtain the spectrum. The data were phased by maximizing the sum of the data points in the real components of the spectrum and fit to the biexponential function $I(\tau) = y_0 + A_f \exp(-\tau/T_{1,f}) + A_s \exp(-\tau/T_{1,s})$. Nutation measurements were performed at three different microwave powers with a nutation pulse of variable length (tipping) pulse followed by a Hahn echo sequence ($t_p - T - \pi/2 - \tau - \pi - \tau -$ echo). Data were collected employing 4-phase cycling, in which in which $\pi/2$ = 16 ns, π = 32 ns and τ = 400 ns for nutation pulse lengths T = 600 ns. The tipping pulse, t_p, is augmented in 4 ns increments from a starting value of 4 ns. Nutation data was processed by subtracting a stretched exponential baseline from the echo decay, then zero-filling with 1024 points, followed by a Fourier transform with a Hamming window.

Other Physical Methods. Cyclic voltammetry measurements were performed with a Metrohm Autolab P128 potentiostat. The electrode configuration consisted of a 2 mm glassy carbon working electrode, a platinum auxiliary electrode and a reference electrode consisting of $Ag/AgNO_3$ (0.01 M in MeCN) incorporated into a

salt bridge containing supporting electrolyte (to minimize Ag^+ leakage). The measurement were collected using a 1 mM solution of [**1**] dissolved in dichloromethane containing 0.1 M $[N(^nBu)_4]PF_6$ as electrolyte. All reduction potentials are referenced versus the ferrocenium/ferrocene ($Fc^{+/0}$) couple. Electronic absorption spectra were recorded on a Shimadzu UVA 3600 spectrophotometer (range 200–1600 nm). Temperature-dependent magnetic susceptibilities were measured by using a SQUID magnetometer (MPMS Quantum Design) at 1.0 T (2–290 K). Underlying diamagnetism was corrected by using tabulated Pascal's constants.[3] Electrospray ionization (ESI) mass spectra were obtained on a Bruker micrOTOF-Q mass spectrometer. Elemental analysis was performed using an EA 1110 CHNS, CE-440 Elemental Analyzer.

Calculations. All calculations in this work were performed with the electronic structure program ORCA.[4] Geometry optimisations were carried out using the BP86 functional with dichloromethane as solvent.[5] A segmented all-electron relativistically contracted basis set of triple-ζ-quality (def2-TZVPP) was used for all atoms.[6] A scalar relativistic correction was applied using the zeroth-order regular approximation (ZORA) method[7] as implemented by van Wüllen.[8] In the context of ZORA, a one centre approximation has been shown to introduce only minor errors to the final geometries. Auxiliary basis sets for all complexes used to expand the electron density in the calculations were chosen to match the orbital basis. The conductor like screening model (COSMO) was used for all calculations.[9] The self-consistent field calculations were tightly converged (1×10^{-8} E_h in energy, 1×10^{-7} E_h in the density change, and 1×10^{-7} in the maximum element of the DIIS[10] error vector). The geometry search for all complexes was carried out in redundant internal coordinates without imposing geometry constraints. The property calculations at the optimised geometries were done with the PBE0 hybrid functional[11] and the RIJCOSX algorithm to expedite calculation of the Hartree-Fock exchange.[12] In this case the same basis sets were used but with enhanced integration accuracy (SPECIALGRIDINTACC 10) for the metal and sulfur atoms. Calculation of **g** and **A** matrices utilised the CP(PPP)[13] basis set for Cu and IGLO-III[14] basis set for sulfur, and employed a larger the integration grid (Grid7) and fully decontracted basis sets.[15]

We used the broken symmetry (BS) approach to describe our computational result of [**1**].[16] We adopt the following notation: the given system was divided into two fragments. The notation BS(*m*,*n*) refers then to a broken symmetry state with *m* unpaired α-spin electrons essentially on fragment 1 and *n* unpaired β-spin electrons localized on fragment 2. In most cases, fragments 1 and 2 correspond to the metal and the ligands,

respectively. In this notation the standard high-spin, open-shell solution is written as BS($m + n$,0). The BS(m,n) notation refers to the initial guess to the wave function. The variational process does, however, have the freedom to converge to a solution of the form BS($m - n$,0) in which effectively the $n\beta$-spin electrons pair up with $n < m\alpha$-spin electrons on the partner fragment. Such a solution is then a standard $M_s \cong (m - n)/2$ spin-unrestricted Kohn-Sham solution. As explained elsewhere,[17] the nature of the solution is investigated from the corresponding orbital transformation (COT) which, from the corresponding orbital overlaps, displays whether the system should be described as a spin-coupled or a closed-shell solution. The exchange coupling constant J was calculated on broken-symmetry geometries using eq. 1,[18] and assuming the spin-Hamiltonian eq. 2 is valid.

$$J = \frac{E_{HS} - E_{BS}}{\langle \hat{S}^2 \rangle_{HS} - \langle \hat{S}^2 \rangle_{BS}} \quad (1)$$

$$\hat{H} = -2J\hat{S}_A \cdot \hat{S}_B \quad (2)$$

Corresponding[17] and canonical orbitals, and density plots were constructed using the program Molekel.[19]

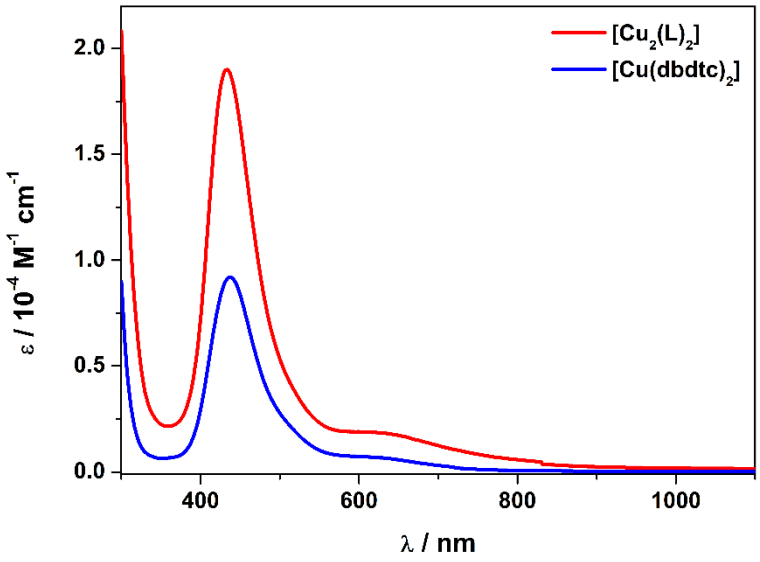

Fig. S1 Overlay of the electronic spectra of [**1**] and [Cu(dbdtc)$_2$] recorded in CH_2Cl_2 solution at ambient temperature.

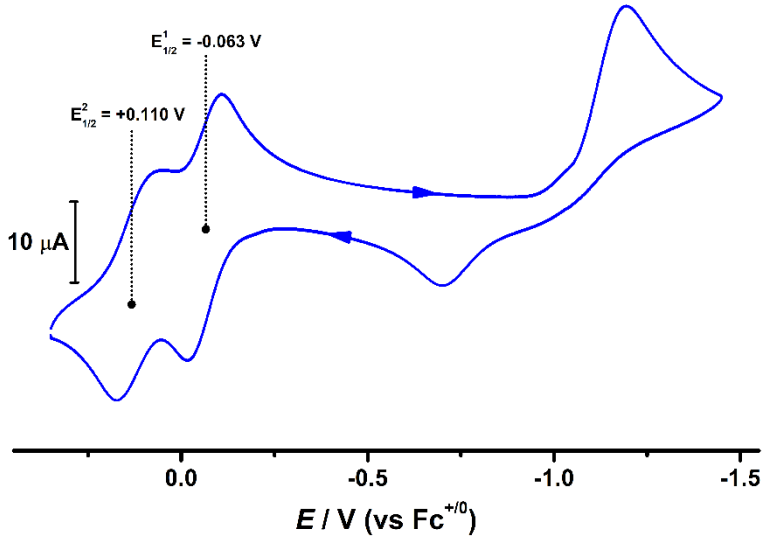

Fig. S2 Cyclic voltammogram of [**1**] in CH_2Cl_2 solution (0.10 M $[N(^nBu)_4]PF_6$ supporting electrolyte) at 22 °C at a scan rate of 100 mV s^{-1}. Potentials are referenced versus the $Fc^{+/0}$ couple.

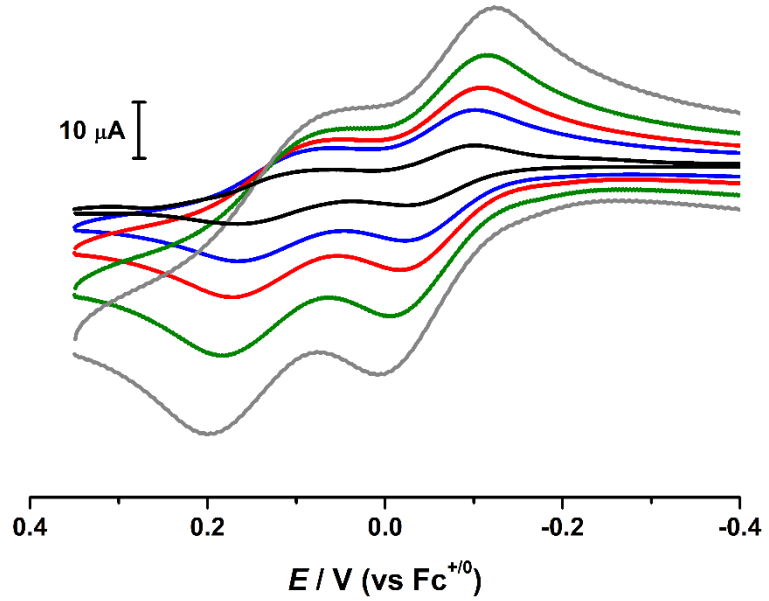

Fig. S3 Cyclic voltammograms of [**1**] in CH_2Cl_2 solution (0.10 M $[N(^nBu)_4]PF_6$ supporting electrolyte) at 22 °C with variable scan rates of 50, 100, 200, 400 and 500 mV s^{-1}. Potentials are referenced versus the $Fc^{+/0}$ couple.

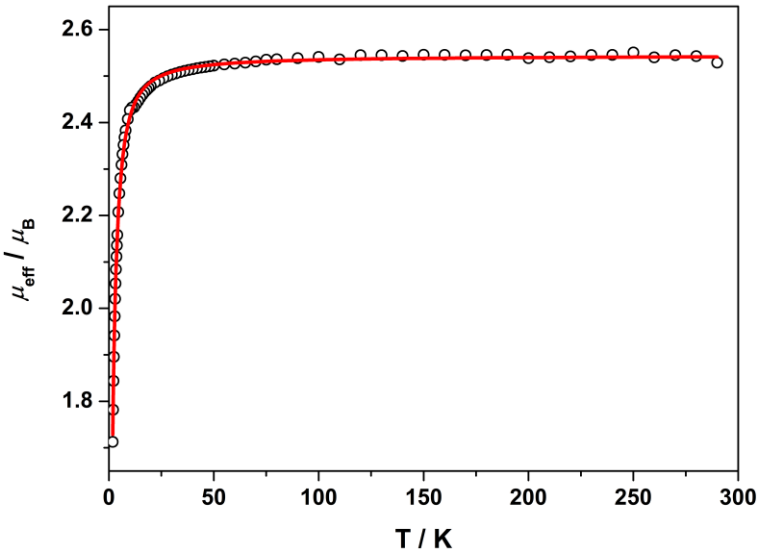

Fig. S4 Temperature dependence of the magnetic moment, μ_{eff}, μ_B, of solid sample of [**1**] in a 1 T external field. Open circles represent the experimental data; the solid line is a best fit using the standard Heisenberg-Dirac-van Vleck Hamiltonian, $\hat{H} = -2JS_1 \cdot S_2 + \mu_B gSH$, gave $J = -0.9$ cm^{-1} (for $S_1 = S_2 = {}^1/_2$) and $g = 2.077$.

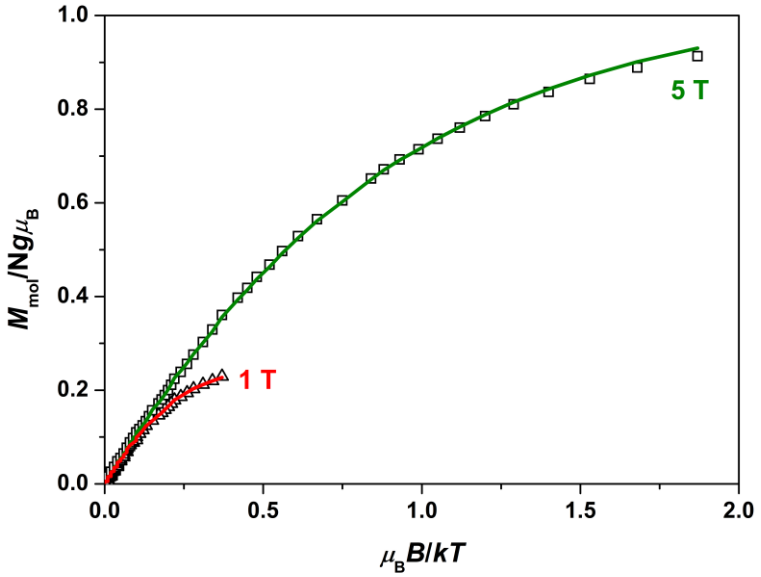

Fig. S5 Magnetisation data recorded on a solid sample of [**1**] at 1 and 5 T. Solid lines represent best fit.

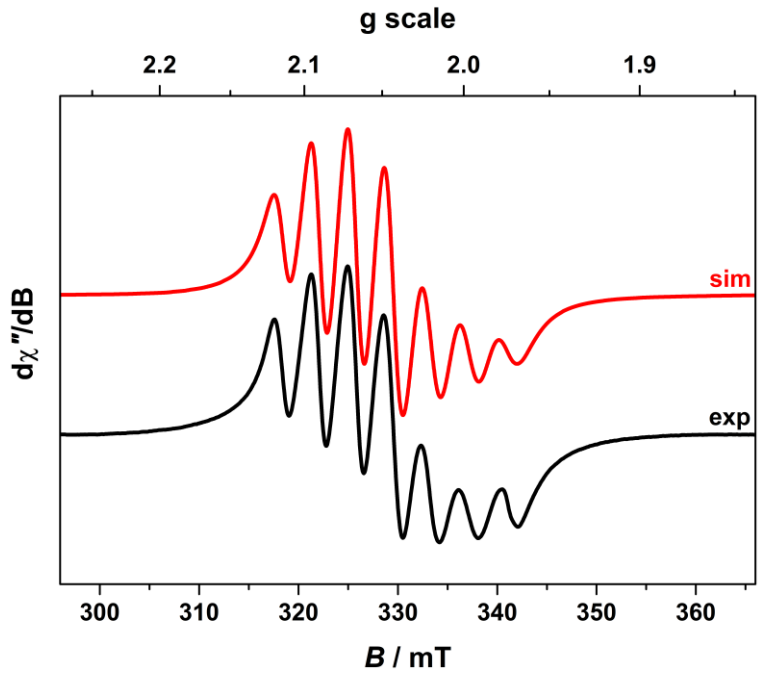

Fig. S6 X-band EPR spectrum of [**1**] recorded in $CHCl_3$ solution at 293 K (experimental conditions: frequency, 9.4230 GHz; modulation, 0.2 mT; power, 0.63 mW). Experimental data are represented by the black line; simulation is depicted by the red trace: $g_{iso} = 2.042$; $A_{iso} = 35 \times 10^{-4}$ cm^{-1} (for $S = 1$ given $J >> A$).

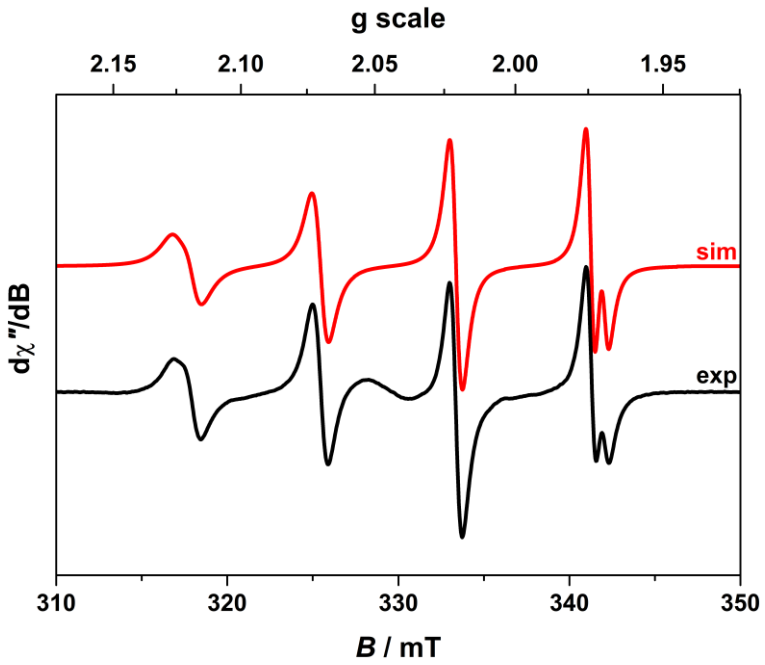

Fig. S7 X-band EPR spectrum of [Cu(dbdtc)$_2$] recorded in $CHCl_3$ solution at 293 K (experimental conditions: frequency, 9.4289 GHz; power, 0.63 mW; modulation, 0.07 mT). Experimental data are represented by the black line; simulation is depicted by the red trace: g_{iso} = 2.043; A_{iso} = 74 × 10^{-4} cm^{-1}.

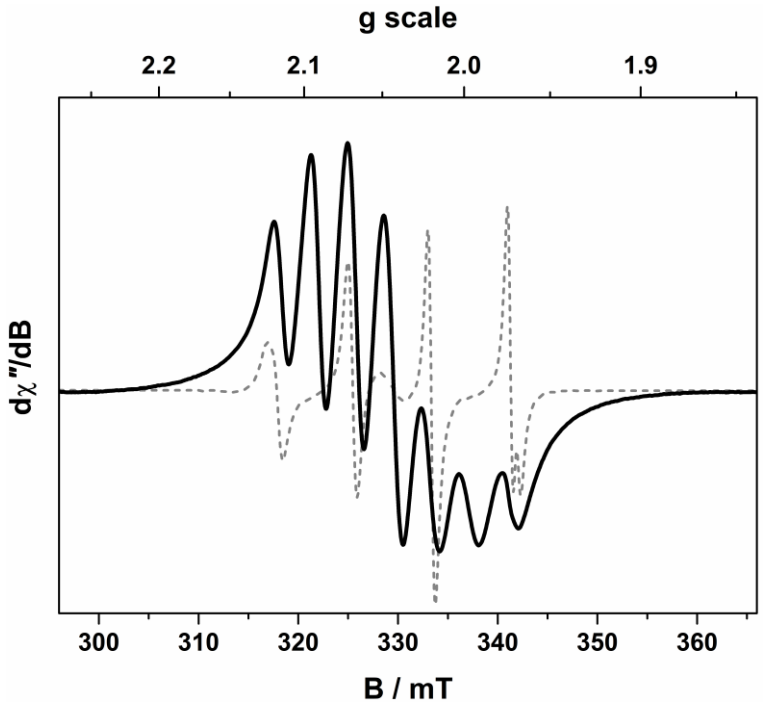

Fig. S8 Overlay of the X-band EPR spectra of [**1**] (solid line) and [Cu(dbdtc)$_2$] (dashed line) recorded in $CHCl_3$ solution at ambient temperature. For [**1**], g_{iso} = 2.042 and $A_{iso} = 35 \times 10^{-4}$ cm^{-1} are obtained from spectral simulation whereas for [Cu(dbdtc)$_2$], g_{iso} = 2.043; $A_{iso} = 74 \times 10^{-4}$ cm^{-1}. Both have the same g-value and spectral width confirming $J >> A$, and therefore the A_{iso} for [Cu(dbdtc)$_2$] is double that for [**1**].

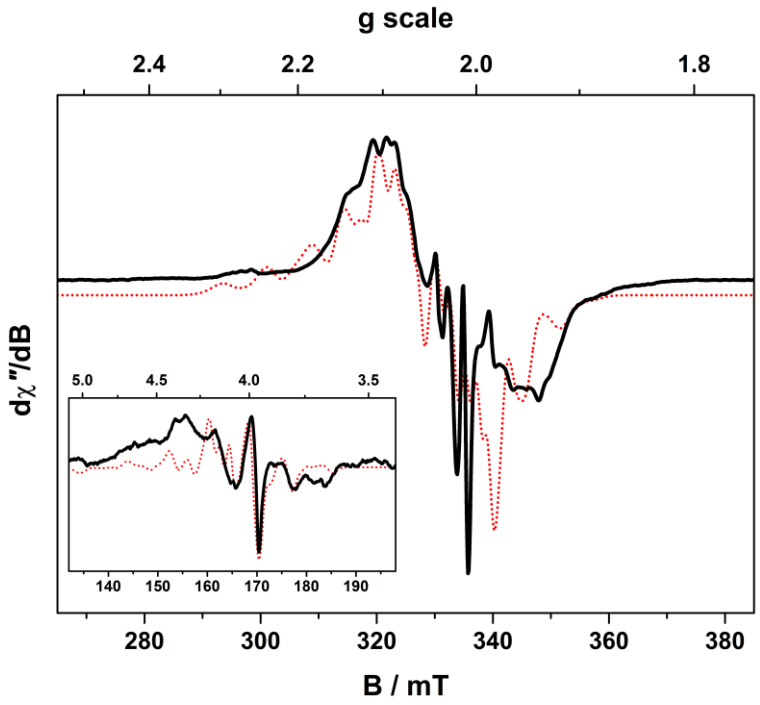

Fig. S9 X-band EPR spectrum of [**1**] recorded in 4:1 $CHCl_3/CH_3CN$ solution at 130 K (experimental conditions: frequency, 9.4317 GHz; modulation, 0.4 mT; power, 2.0 mW). Inset shows half-field signal (conditions: frequency 9.4316 GHz; power 99.5 mW; modulation 0.7 mT). Experimental data are represented by the black line; simulation is depicted by the dotted red trace: g = (2.03, 2.03, 2.10); A = (–30, –30, –160) × 10^{-4} cm^{-1}; J = +0.1 cm^{-1}; ϕ = 58°; θ = 0° (for $r_{Cu\cdots Cu}$ = 6 Å).

The simulation necessitated the full interaction Hamiltonian for a pair of weakly interacting spins is defined as:

$$\hat{H} = \hat{H}_1 + \hat{H}_2 + \hat{H}_{int}$$

where $\hat{H}_1$ and $\hat{H}_2$ are Hamiltonians for the independent spins 1 and 2. The $\hat{H}_{int}$ term is the interaction Hamiltonian which accounts for the isotropic exchange, anti-symmetric exchange and the anisotropic spin–spin (dipole–dipole coupling) interactions between a pair of paramagnetic centers.[20] The full Hamiltonian is given by:

$$\hat{H} = \mathbf{S}_1 \cdot \mathbf{J} \cdot \mathbf{S}_2 + \mu_B \sum_{i=1,2} \mathbf{S}_i \cdot \mathbf{g}_i \cdot \mathbf{B} + \sum_{i=1,2} \mathbf{S}_i \cdot \mathbf{A} \cdot \mathbf{I}_i$$

As antisymmetric exchange can be neglected, the J-matrix of the interaction term is composed of the isotropic exchange interaction, J, and an anisotropic dipolar interaction, $\mathbf{J_d}$, which is the traceless anisotropic coupling matrix. The interaction term is therefore defined as:

$$\widehat{H}_{int} = \mathbf{S}_1 \cdot (\mathbf{J_d} - 2J \cdot \mathbf{1}) \cdot \mathbf{S}_2$$

where the coupling between the two Cu centres is dependent on the interspin distance ($r_{Cu\cdots Cu}$) and the angle the *z*-axis of the second site, normal to the CuS_4 coordination plane, makes with the interspin vector with respect to the first Cu centre. Conveniently this comes "built-in" to the *Xsophe* program.[2] Therefore the two Cu centres in [**1**] have different diagonal reference frames, their principal **g** and **A** matrices point in different directions such that a 3×3 transformation matrix is needed to describe the angles between their principal axes. These are related to the orientation of the dipolar exchange matrix defined by the interspin distance ($r_{Cu\cdots Cu}$) through a further set of Euler angles. Without any symmetry constraints, this generates a huge number of parameters. The simulation of [**1**] was tackled assuming the geometry-optimised structure reflected the structure of the molecule in (frozen) solution. Assuming local axial symmetry at each Cu centre, the unique g_{zz} and A_{zz} for individual ions are normal to their respective CuS_4 coordination planes. The optimised structure aligns the Cu···Cu vector at an angle of ϕ = 40.6° to the z_1 and z_2 normals of each coordination plane. The coordination plane at each Cu site are parallel (θ = 0°). Therefore one Euler angle (ϕ) was included in the simulation to transpose the unique principal axes of the individual Cu centres, with the value of 40.6° from the optimised structure used as a starting point, along with the *g*- and *A*-values from $[Cu(dbdtc)_2]$ (Fig. S10). The simulation assessed each parameter of the *J*-matrix as well as the *g*- and *A*-matrices to settle on a fit that encompassed the spectral width of the signal. For *g* = (2.03, 2.03, 2.10), ϕ = 58°, and $r_{Cu\cdots Cu}$ = 6 Å, then

$$\mathbf{J}_\mathrm{d} = \begin{bmatrix} -85.618 & 0 & -115.205 \\ 0 & 92.603 & 0 \\ -115.205 & 0 & 23.928 \end{bmatrix} \times 10^{-4}$$

The variation of ϕ on the resultant simulation for the allowed transitions is shown in Fig. S11. Given the limited spectral resolution of this sample in frozen solution, these spin-Hamiltonian parameters do not represent a unique solution. The assessment of the best fit is improved by the good match of the spectral features of the half-field signal in terms of the central line and the width of the spectrum. The line shape is influenced by *g*-, *A*- and *J*-strain due to the structural inhomogeneity throughout the sample which will vary widely due to the inherent flexibility of the metallo-macrocycle, and cannot be modelled. The field-swept echo-detected spectrum was simulated using identical spin-Hamiltonian parameters, though linewidths and strain parameters were varied to capture the spectral profile. Comparisons of the ESE and continuous wave spectra are presented in Fig. S12.

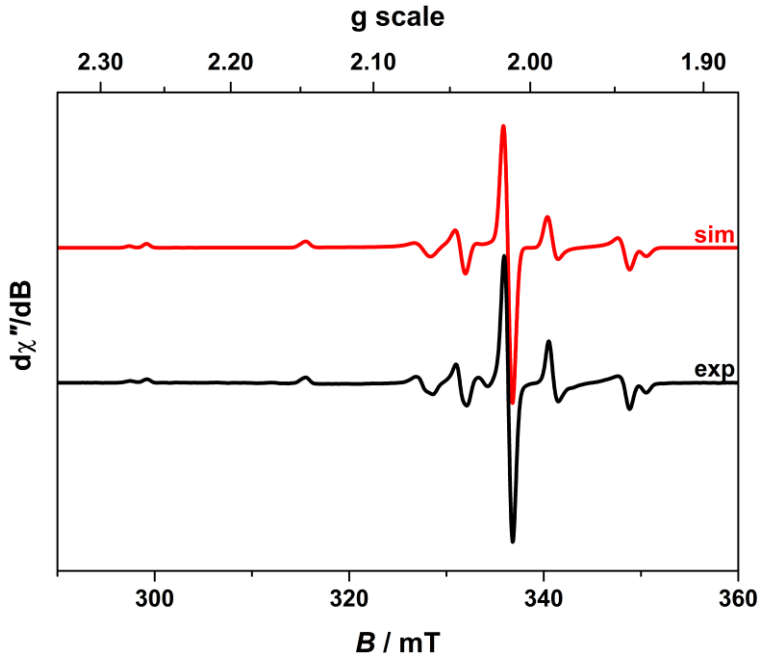

Fig. S10 X-band EPR spectrum of [Cu(dbdtc)$_2$] recorded in $CHCl_3$/CH_3CN solution at 130 K (experimental conditions: frequency, 9.4786 GHz; power, 0.63 mW; modulation, 0.4 mT). Experimental data are represented by the black line; simulation is depicted by the red trace: g = (2.023, 2.024, 2.090); A = (–38, –40, –161) × 10^{-4} cm^{-1}.

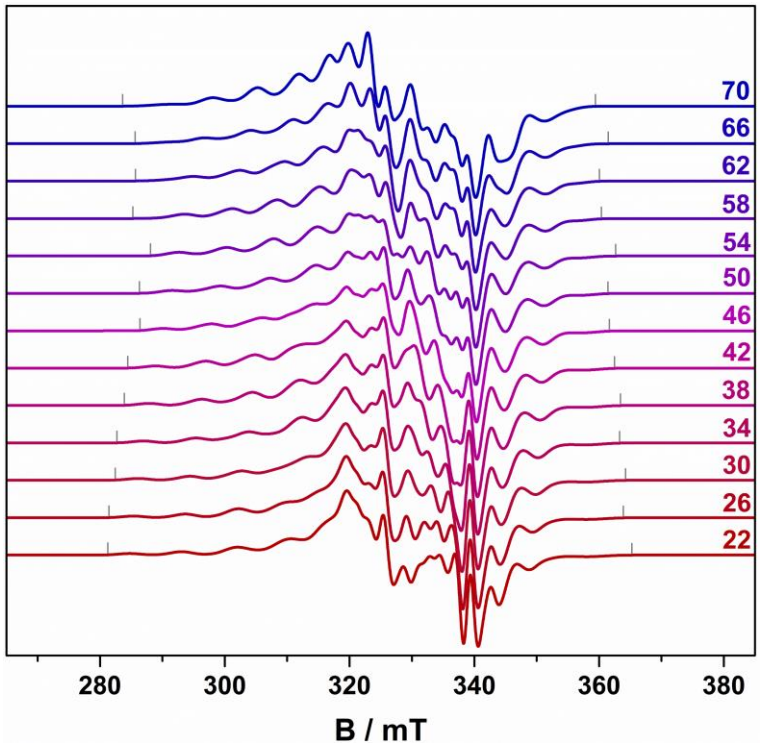

Fig. S11 Variation of the simulated continuous wave X-band EPR spectrum of [**1**] as a function of the ϕ angle, ranging 22°–70° as indicated. The vertical grey lines mark the width of the simulation used to match the experimental spectrum.

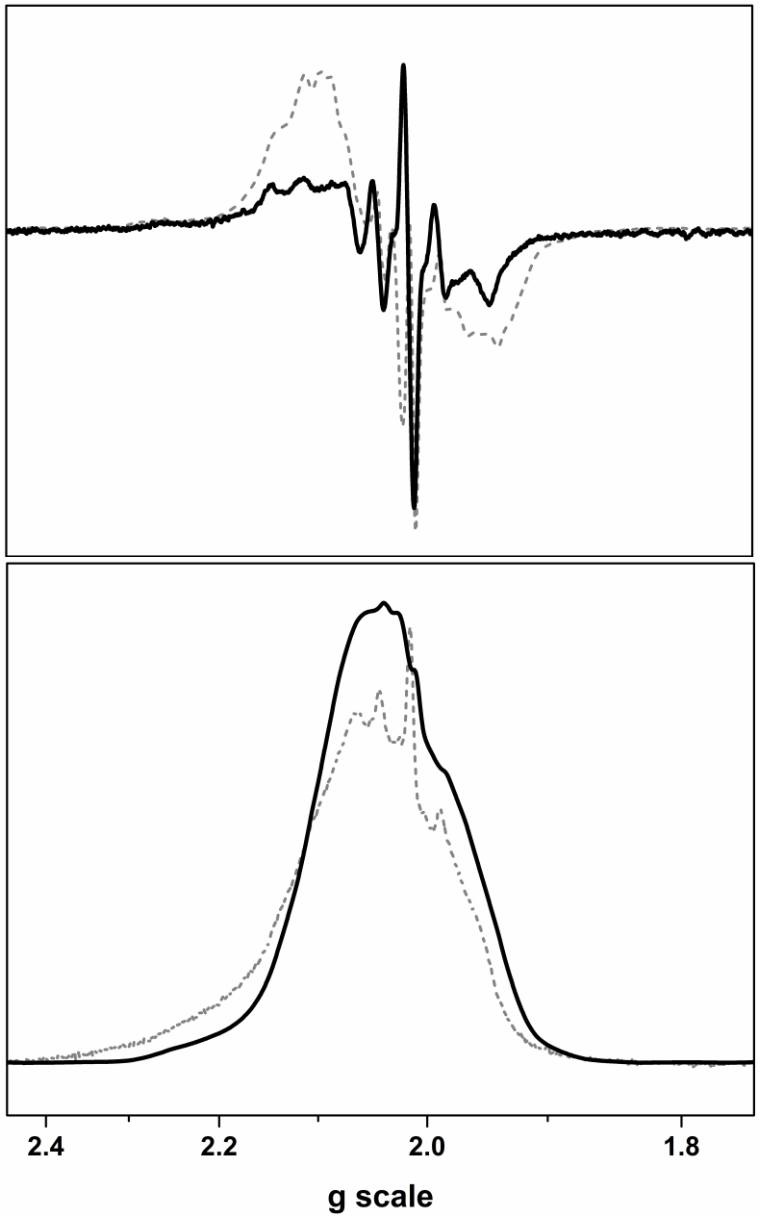

Fig. S12 Overlay of the ESE detected and continuous wave (CW) spectra of [**1**]. Top: in derivative mode with ESE as solid line; CW as dashed trace. Bottom: in absorption mode with CW as solid line; ESE as dashed trace.

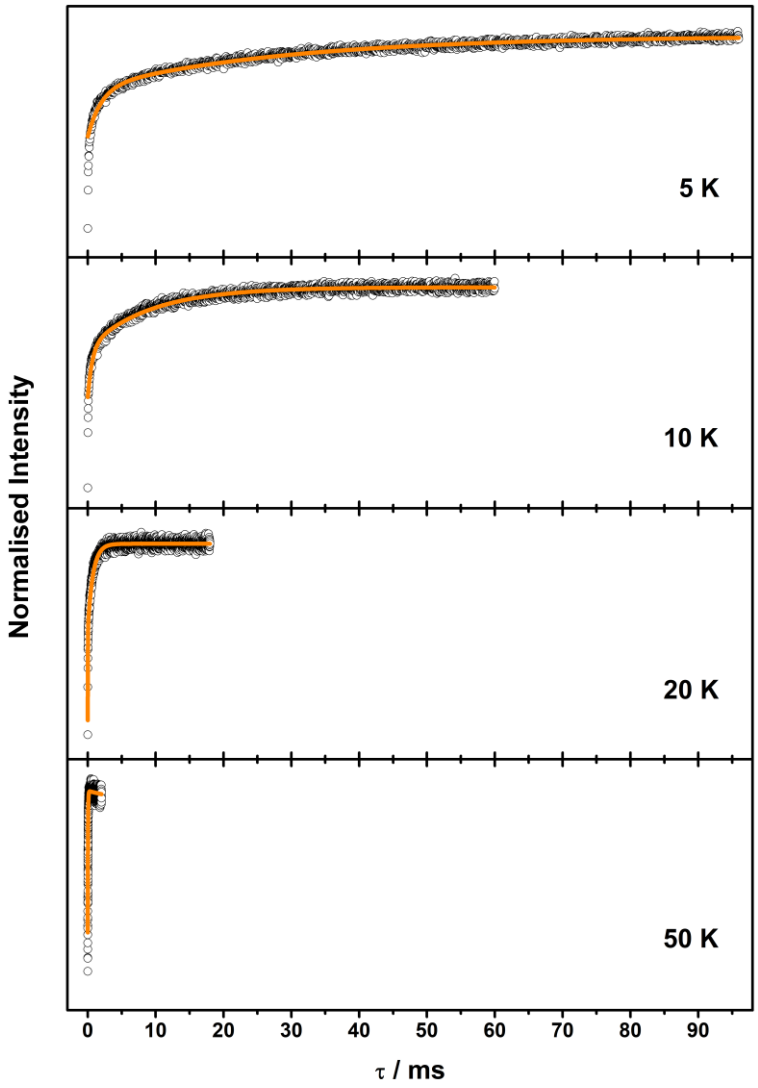

Fig. S13 Inversion recovery data (open circles) and biexponential fit (solid line) of a 0.5 mM solution of [**1**] in 4:1 $CDCl_3/Cl_3CCN$ recorded over the temperature range 5 – 50 K. Fit parameters are given in Table S1.

Table S1 Biexponential fit functions for inversion recovery curves of [**1**], B_0 = 350 mT

T / K	A_f	$T_{1,f}$ / μs	A_s	$T_{1,s}$ / μs
5	0.190(3)	1230(3)	0.175(1)	25100(30)
10	0.228(5)	1210(6)	0.334(4)	10000(10)
20	1.47(4)	21(1)	1.36 (1)	7640(80)
50	14.2(1)	37.9(4)	4.0(9)	2500(90)

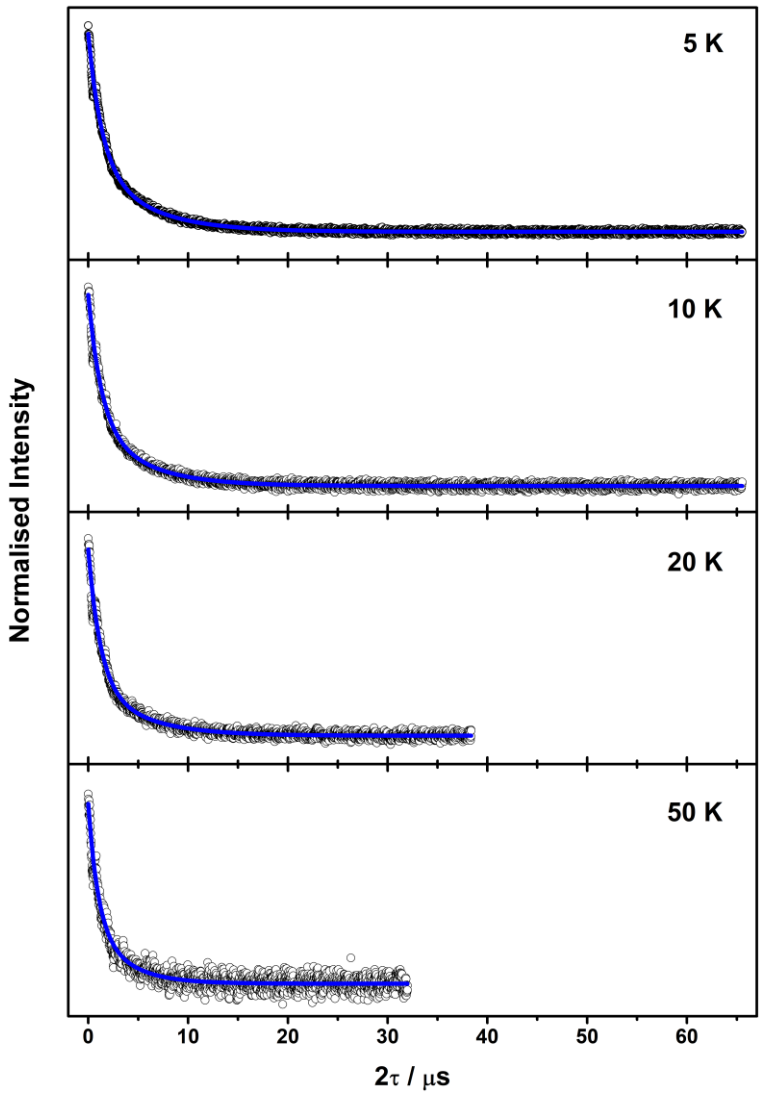

Fig. S14 Hahn-echo decay curves (open circles) and biexponential fit (solid line) of a 0.5 mM solution of [**1**] in 4:1 $CDCl_3/Cl_3CCN$ recorded over the temperature range 5 – 50 K. Fit parameters are given in Table S2.

Table S2 Biexponential fit functions for Hahn-echo decay curves of [**1**], B_0 = 350 mT

T / K	A_f	$T_{M,f}$ / μs	A_s	$T_{M,s}$ / μs
5	28.8(3)	1.35(2)	16.7(3)	5.35(7)
10	34.0(2)	1.30(1)	18.3(1)	5.03(5)
20	94(2)	1.22(3)	39(2)	5.0(2)
50	105.0(3)	0.97(2)	59.2(2)	3.36(12)

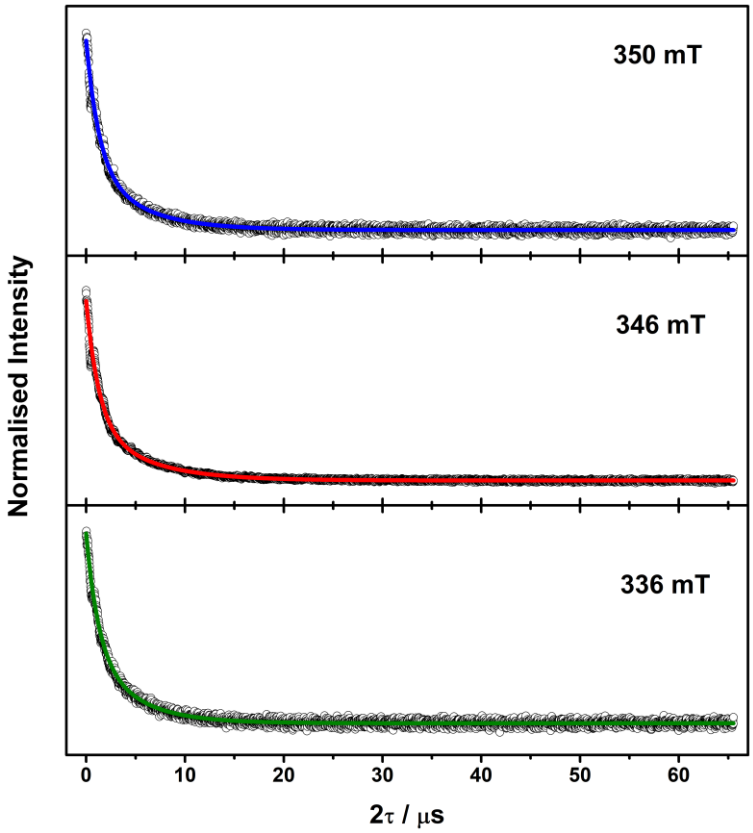

Fig. S15 Hahn-echo decay curves (open circles) and biexponential fit (solid line) of a 0.5 mM solution of [**1**] in 4:1 $CDCl_3/Cl_3CCN$ as a function of magnetic field, B_0. Fit parameters are given in Table S3.

Table S3 Biexponential fit functions for Hahn-echo decay curves of [**1**] as a function of field

B_0 / mT	A_f	$T_{M,f}$ / μs	A_s	$T_{M,s}$ / μs
336	53.6(2)	1.23(2)	37.6(1)	4.35(2)
346	49.1(4)	1.28(2)	24.2(5)	5.52(7)
350	34.0(2)	1.30(1)	18.3(1)	5.03(5)

Table S4 Geometry-optimised coordinates for [**1**]

Cu	0.00000	0.00000	0.00000
Cu	-0.06314	-3.87226	-4.52351
S	1.79517	-2.41359	-4.65461
S	1.85416	-1.45872	0.14033
S	1.78753	-5.34200	-4.48541
S	1.85033	1.45393	-0.14338
S	-1.85779	-1.45952	0.12937
S	-1.91736	-2.41381	-4.66554
S	-1.85121	1.46911	-0.03488
S	-1.91366	-5.32612	-4.37907
C	2.71646	-3.88300	-4.59295
N	4.07152	-3.90090	-4.62377
C	4.82201	-5.16413	-4.57150
H	5.78119	-4.95643	-4.05010
H	4.24909	-5.87164	-3.93648
C	5.07588	-5.78595	-5.95473
H	5.61037	-5.05376	-6.59950
H	4.09245	-5.97358	-6.43622
C	5.87913	-7.08732	-5.86543
H	5.34797	-7.84779	-5.25609
H	6.04665	-7.52440	-6.87005
H	6.87550	-6.92582	-5.40116
C	2.78542	0.00000	-0.00000
N	4.14240	0.00242	-0.00201
C	4.92207	1.24162	-0.15657
H	4.21780	2.02633	-0.49867
H	5.65648	1.07490	-0.97439
C	5.65122	1.69609	1.12064
H	6.42762	0.94867	1.39832
H	6.21688	2.61492	0.85104
C	4.73504	1.97110	2.31717
H	3.97915	2.74632	2.07940
H	5.31982	2.31640	3.19381
H	4.18001	1.06064	2.62398
C	4.91358	-1.24727	0.11739
H	4.19386	-2.04438	0.39557
H	5.63084	-1.13882	0.95801
C	5.66141	-1.61736	-1.15298
C	7.07189	-1.61645	-1.18072
H	7.63416	-1.35561	-0.26924
C	7.76194	-1.94728	-2.35720
H	8.86275	-1.94212	-2.37086
C	7.04614	-2.28414	-3.51689
H	7.58779	-2.53918	-4.44240
C	5.63559	-2.29528	-3.51054
C	4.95259	-1.95959	-2.32317
H	3.84960	-1.96451	-2.30994
C	4.86142	-2.66685	-4.76472
H	4.15187	-1.85934	-5.04072
H	5.56421	-2.79907	-5.61493
C	-2.77967	0.00975	0.07171
N	-4.13465	0.02723	0.10514
C	-4.88559	1.29048	0.05670
H	-5.84598	1.08357	-0.46272
H	-4.31441	1.99922	-0.57859
C	-5.13617	1.91019	1.44157
H	-5.66920	1.17703	2.08646
H	-4.15174	2.09725	1.92105
C	-5.93956	3.21186	1.35568
H	-5.40960	3.97309	0.74614
H	-6.10507	3.64792	2.36112
H	-6.93680	3.05090	0.89323

C	-2.84871	-3.87219	-4.52256
N	-4.20571	-3.87442	-4.51860
C	-4.98523	-5.11354	-4.36261
H	-4.28068	-5.89806	-4.02061
H	-5.71896	-4.94635	-3.54427
C	-5.71548	-5.56875	-5.63893
H	-6.49211	-4.82133	-5.91654
H	-6.28109	-6.48745	-5.36821
C	-4.80014	-5.84450	-6.83604
H	-4.04418	-6.61978	-6.59837
H	-5.38558	-6.19008	-7.71206
H	-4.24507	-4.93428	-7.14373
C	-4.97683	-2.62467	-4.63741
H	-4.25703	-1.82748	-4.91510
H	-5.69416	-2.73246	-5.47806
C	-5.72448	-2.25505	-3.36681
C	-7.13489	-2.25511	-3.33914
H	-7.69726	-2.51521	-4.25078
C	-7.82473	-1.92433	-2.16258
H	-8.92550	-1.92882	-2.14898
C	-7.10878	-1.58842	-1.00271
H	-7.65030	-1.33341	-0.07713
C	-5.69830	-1.57817	-1.00896
C	-5.01550	-1.91374	-2.19644
H	-3.91255	-1.90938	-2.20955
C	-4.92398	-1.20730	0.24535
H	-4.21407	-2.01469	0.52075
H	-5.62668	-1.07579	1.09572

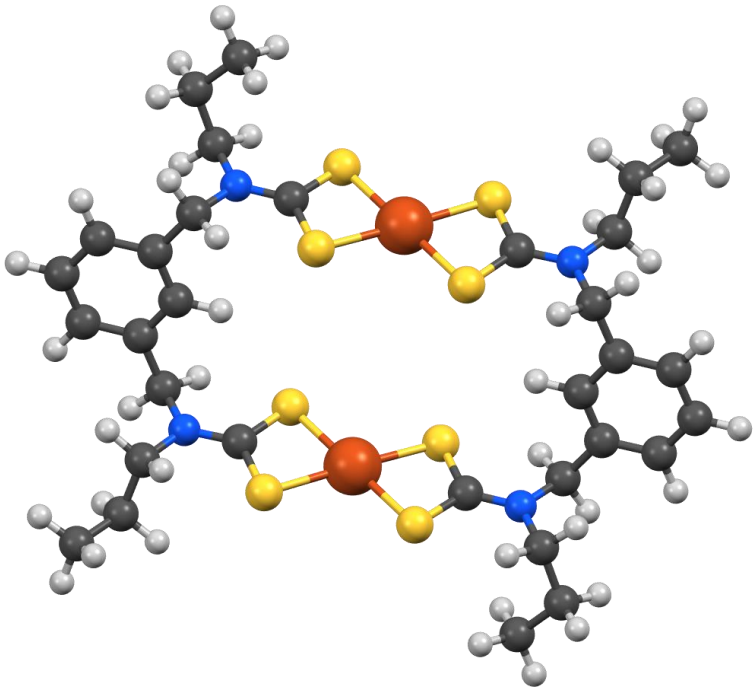

Fig. S16 Geometry-optimised structure of [**1**]

Table S4 Comparison of calculated and experimental metric parameters[a]

	Calculated	**Experimental**[b]
avg. Cu–S	2.363	2.296(2)
Cu(1)···Cu(2)	5.955	5.421(3)[c]
avg. S–Cu–S	76.6	77.62(4)
α[d]	2.8	8.1
θ[e]	0.0	0.0
ϕ[f]	40.6	52.1

[a] Distances in angstrom; angles in degrees; number in parenthesis denotes the Cu(1) and Cu(2) sites. [b] Data obtained from refs [21] and [22]. [c] Intermetallic distances from the dicopper(III) doubly-oxidised metallo-macrocycle from ref. [22]. [d] Dihedral angle between CuS_2 planes. [e] Dihedral angle between CuS_4 mean planes. [f] Angle between Cu···Cu vector and CuS_4 mean plane.

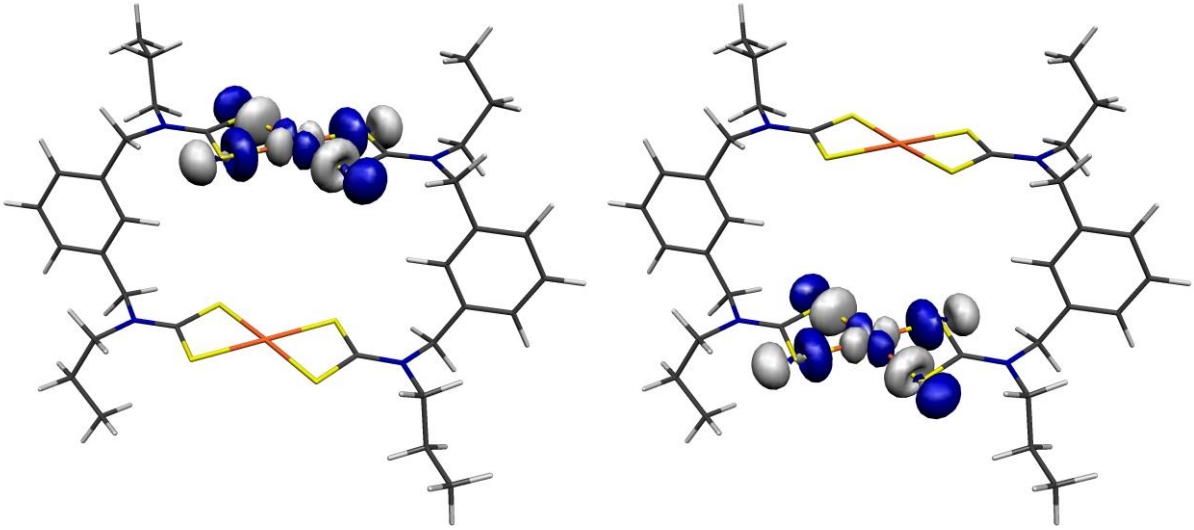

Fig. S17 Magnetic orbitals of [**1**] derived from spin-unrestricted BS(1,1) DFT calculations

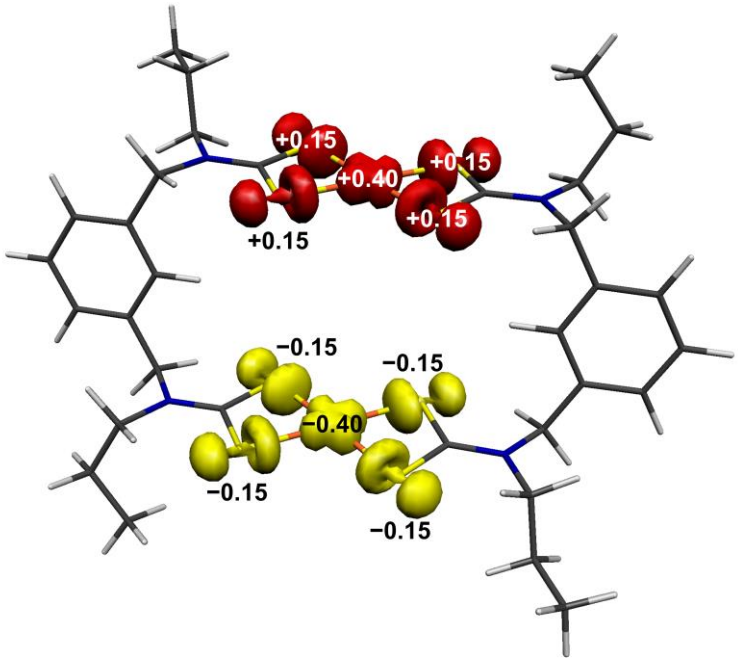

Fig. S18 Mulliken spin density plot for [**1**] spin unrestricted BS(1,1) DFT calculations (red: α-spin, yellow: β-spin).

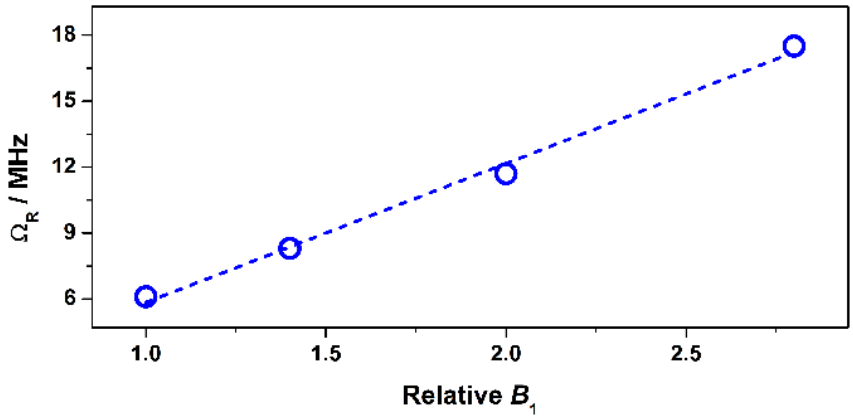

Fig. S19 Linear dependence of Ω_R with respect to the B_1 field for [**1**] in 4:1 $CDCl_3/Cl_3CCN$ at 10 K and 350 mT. Dashed trace represents line of best fit.

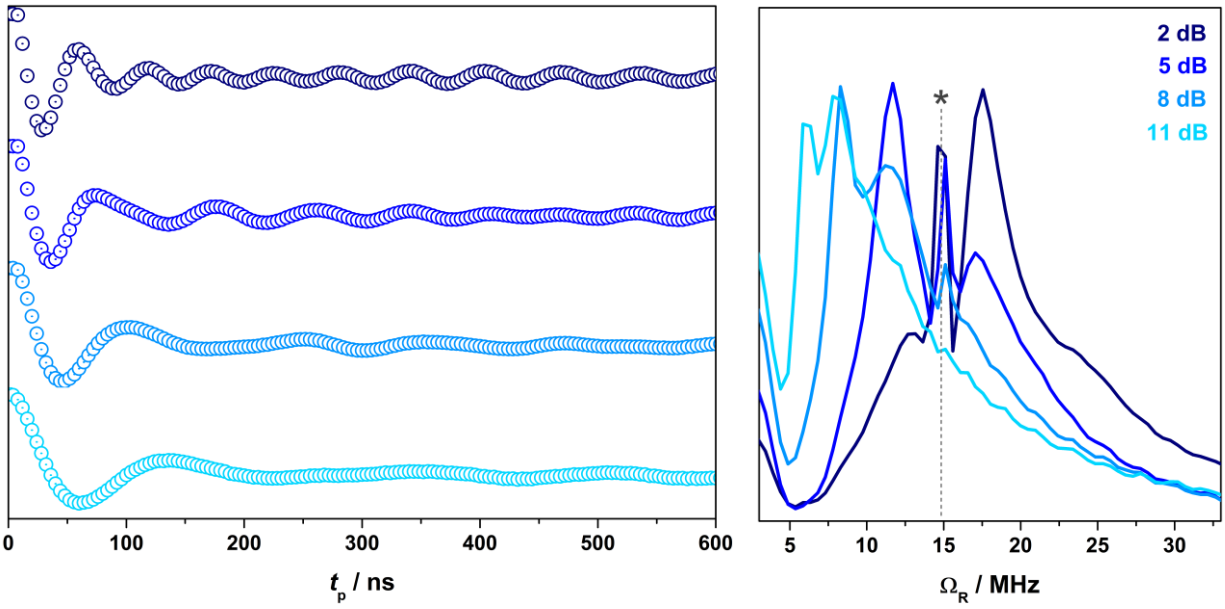

Fig. S20 Rabi oscillations (left) and corresponding frequencies from the Fourier transfer of the data (right) for [**1**] in 4:1 $CDCl_3/Cl_3CCN$ at 10 K and 343.5 mT from variable power nutation measurements. The asterisk in the Fourier transform data indicate the peak matching the Larmor frequency of ^1H (14.7 MHz) within error.[23]

References

1 P. A. Ajibade, B. M. Sikakane, N. L. Botha, A. E. Oluwalana and B. Omondi, *J. Mol. Struct.*, 2020, **1221**, 128791.

2 G. R. Hanson, K. E. Gates, C. J. Noble, M. Griffin, A. Mitchell and S. Benson, *J. Inorg. Biochem.*, 2004, **98**, 903.

3 G. A. Bain and J. F. Berry, *J. Chem. Educ.*, 2008, **85**, 532.

4 F. Neese, *WIREs Comput. Molec. Sci.*, 2012, **2**, 73.

5 (*a*) A. D. Becke, *J. Chem. Phys.*, 1988, **84**, 4524; (*b*) J. P. Perdew, *Phys. Rev. B*, 1986, **33**, 8822.

6 D. A. Pantazis, X.-Y. Chen, C. R. Landis and F. Neese, *J. Chem. Theory Comput.*, 2008, **4**, 908.

7 (*a*) E. van Lenthe, J. G. Snijders and E. J. Baerends, *J. Chem. Phys.*, 1996, **105**, 6505; (*b*) E. van Lenthe, A. van der Avoird and P. E. S. Wormer, *J. Chem. Phys.*, 1998, **108**, 4783; (*c*) J. H. van Lenthe, S. Faas and J. G. Snijders, *Chem. Phys. Lett.*, 2000, **328**, 107.

8 C. J. van Wüllen, *J. Chem. Phys.*, 1998, **109**, 392.

9 A. Klamt and G. Schüüramann, *J. Chem. Soc., Perkin Trans. 2*, 1993, 799.

10 (*a*) P. Pulay, *Chem. Phys. Lett.*, 1980, **73**, 393; (*b*) P. Pulay, *J. Comput. Chem.*, 1982, **3**, 556.

11 (*a*) J. P. Perdew, K. Burke and M. Ernzerhof, *Phys. Rev. Lett.*, 1996, **77**, 3865; (*b*) C. Adamo and V. Barone, *J. Chem. Phys.*, 1999, **110**, 6158.

12 (*a*) F. Neese, F. Wennmohs, A. Hansen and U. Becker, *Chem. Phys.*, 2009, **356**, 98; (*b*) R. Izsák and F. Neese, *J. Chem. Phys.*, 2011, **135**, 144105.

13 F. Neese, *Inorg. Chim. Acta*, 2002, **337**, 181.

14 K. U. Fleischer and M. Schindler, *The IGLO-Method: Ab Initio Calculationn and Interpretation of NMR Chemical Shifts and Magnetic Susceptibilities*, Springer-Verlag, Heidelberg, 1990.

15 (*a*) F. Neese, *J. Chem. Phys.*, 2001, **115**, 11080; (*b*) F. Neese, *J. Chem. Phys.*, 2003, **118**, 3939.

16 (*a*) L. Noodleman, *J. Chem. Phys.*, 1981, **74**, 5737; (*b*) L. Noodleman, D. A. Case and A. Aizman, *J. Am. Chem. Soc.*, 1988, **110**, 1001; (*c*) L. Noodleman and E. R. Davidson, *Chem. Phys.*, 1986, **109**, 131; (*d*) L. Noodleman, J. G. Norman, J. H. Osborne, A. Aizman and D. A. Case, *J. Am. Chem. Soc.*, 1985, **107**, 3418; (*e*) L. Noodleman, C. Y. Peng, D. A. Case and J. M. Monesca, *Coord. Chem. Rev.*, 1995, **144**, 199.

17 F. Neese, *J. Phys. Chem. Solids*, 2004, **65**, 781.

18 (*a*) T. Soda, Y. Kitagawa, T. Onishi, Y. Takano, Y. Shigetu, H. Nagao, Y. Yoshioka and K. Yamaguchi, *Chem. Phys. Lett.*, 2000, **319**, 223; (*b*) K. Yamaguchi, Y. Takahara and T. Fueno, in *Applied Quantum Chemistry*, ed. V. H. Smith, Reidel, Dordrecht, The Netherlands, 1986, p. p. 155.

19 *Molekel*, Advanced Interactive 3D-Graphics for Molecular Sciences, Swiss National Supercomputing Center. https://ugovaretto.github.io/molekel/

20 (*a*) T. D. Smith and J. R. Pilbrow, *Coord. Chem. Rev.*, 1974, **13**, 173; (*b*) J. F. Boas, P. R. Hicks, J. R. Pilbrow and T. D. Smith, *J. Chem. Soc., Faraday Trans. 2*, 1978, 417; (*c*) S. S. Eaton and G. R. Eaton, *J. Am. Chem. Soc.*, 1982, **104**, 5002; (*d*) S. S. Eaton, K. M. More, B. M. Sawant and G. R. Eaton, *J. Am.*

Chem. Soc., 1983, **105**, 6560; (*e*) R. Damoder, K. M. More, G. R. Eaton and S. S. Eaton, *J. Am. Chem. Soc.*, 1983, **105**, 2147.

21 J. Cookson, E. A. L. Evans, J. P. Maher, C. J. Serpell, R. L. Paul, A. R. Cowley, M. G. B. Drew and P. D. Beer, *Inorg. Chim. Acta*, 2010, **363**, 1195.

22 P. D. Beer, N. Berry, M. G. B. Drew, O. D. Fox, M. E. Padilla-Tosta and S. Patell, *Chem. Commun.*, 2001, 199.

23 S. R. Hartmann and E. L. Hahn, *Phys. Rev.*, 1962, **128**, 2042.